Investigation of the mixing characteristics in a transverse hydrogen injection combustor with an inlet compression ramp

ZHAO, Majie, LI, Qinling <http://orcid.org/0000-0002-7191-9538> and YE, Taohong

Investigation of the Mixing Characteristics in a Transverse Hydrogen Injection Combustor with an Inlet Compression Ramp

Majie Zhao[a], Qinling Li[b] & Taohong Ye[a,*]

[a] Department of Thermal Science and Energy Engineering, University of Science and Technology of China, Hefei, 230027, P.R. China

b Department of Engineering and Mathematics/MERI, Sheffield Hallam University, S1 1WB, United Kingdom

Abstract:

A shock-enhanced mixing in a transverse hydrogen injection combustor with an inlet compression ramp is carried out by using Large-eddy simulation (LES). Effects of a shock train induced by the inlet compression ramp on the mixing process have been investigated at three jet to cross-flow momentum flux ratios, *J*. The counter-rotating vortex pairs (CVP), promoting the mixing process of the fuel jet plume and mainstream air, is significantly affected by the reflected shock. The vorticity analysis is constructed to further understand the turbulent mixing mechanism. The shock-induced baroclinic torque is found to play an important role on the generation of the vorticity in the near field of the fuel jet, and the place where the reflected shock interacts with the jet plume. In addition, the probability density function (PDF) of mixture fraction is also investigated.

Key words: Large eddy simulation, Turbulent mixing, Hydrogen jet in supersonic cross-flow, Shock-induced mixing

1. Introduction

Since the residence time of fuel and air is of the order of millisecond, the fast and efficient mixing process is the key issue in the scramjet combustor design [1]. The fuel jet in supersonic cross-flow (JISCF), a typical combustor structure designed for high efficient mixing and combustion in the scramjet engine, has been studied by many researchers [2-6]. The interactions between the fuel jet plume, the large-scale coherent structures and shock waves in the scramjet combustor, have significant effects on the mixing process and flame stabilization [7]. Therefore, it is of great importance to study the mixing mechanism in the JISCF combustor for the practical engineering applications and gas dynamics.

Different from the jet in low Mach number cross-flow with the mainly dependent parameter being of Reynolds number [8], the study of JISCF is a multi-objective variable problem, including jet to cross-flow momentum flux ratio, geometry, the number of the jet orifice and the jet flow angle [9-11]. Shock wave and compressibility have been found to have great impacts on the mixing process in JISCF combustor. For instances, the higher compressibility of the shear layer vortex is not conducive to the mixing process [12]. On the other hand, the interaction between the sudden pressure change due to shock wave and that of density on the interface of the light / heavy gas, such as the flow of hydrogen

surrounded by air, will produce vortex structures and thus enhance the mixing process [13]. Although the presence of shock waves leads to total pressure loss in a scramjet combustor, it has positive effects on the fuel/air mixing and combustion processes in a supersonic combustion [7,14-16]. Aso et al [17] studied the effect of the pressure ratio of jet to supersonic cross-flow on the mixing process by using the Schlieren photography. The bow shock, Mach disk, barrel shock and recirculation zone upstream of the fuel jet became larger with the increasing pressure ratio. The detailed velocity field induced by a sonic jet injected into a Mach 1.6 supersonic cross-flow were obtained by Santiago & Dutton 1997 [18] with Schlieren photography and Laser Doppler Velocimetry (LDV). Gruber, Nejadt & Chen [19] and Gruber et al [20] studied the penetration and mixing characteristics of the jet in supersonic cross-flow using two-dimensional Planar Mie-scattering techniques. The detailed characteristics of the transient reaction zone in the supersonic cross-flow combustor were studied by Gamba and Mungal [21] using OH-PLIF imaging techniques. It was found that the ignition characteristics were strongly affected by the jet momentum ratio, and the flame was stabilized by the recirculation zone upstream of the fuel jet. Mai et al. [7] studied the effects of the interaction of oblique shock and supersonic transverse jet on mixing and combustion process. The results show that the presence of oblique shocks has a significant effect on the mixing of fuel and air in the recirculation zone downstream the injection slot. Meanwhile the residence time of the mixture and the recirculation zone downstream of fuel jet slot increases which contributes to the flame stabilization. Characteristics of the mixing and combustion process in the supersonic transverse circular jet and rhombic jet combustion chamber were studied by Kobayashi et al. [22]. Rubins et al. [15] shows that ignition can occur at relatively low temperature when the shock acts on the shear layer, and the fuel jet is parallel to the air stream. Chaudhuri et al. [23] suggested that the interaction between the oblique shock wave and the mixing shear layer can increase the growth rate of the thickness of the mixed layer. The study of shock wave and supersonic mixing layer by Huete et al. [24 &25] demonstrated that shock waves can promote the ignition of supersonic mixing layers. The study of Nakamura et al [16] indicates that the interaction between oblique shock and the fuel jet can increase the extinction limit of the combustion chamber in the supersonic transverse jet. The effects of oblique shock waves on the mixing process in a supersonic transverse jet was studied by Huang et al. [26] using RANS. The boundary layer separation regions up- and down-stream of the jet orifice increased with the high oblique wave intensity, which promoted the mixing of fuel jet and air. However, the mechanism of interaction between the oblique shock wave and the transverse fuel jet, the promotion of the fuel/air mixing and the impact on the combustion process are still not very clear in JISC combustor, which motivate the current work.

Computational fluid dynamics (CFD) plays an increasing role in the development of scramjet technology with the rapidly developed modern computer facility. Based on the experiments of Santiago [18] and Beresh [27], Chai [28] provided the instantaneous flow field structures using large eddy

simulation (LES). It is pointed out that the dominant oscillatory frequency of the bow shock and upwind side barrel shock is St = 0.3 for the sonic jet supersonic cross-flow. While for supersonic jet in subsonic cross-flow, the flow is dominated by the roll up of upwind side shear layer. Rana et al. [29] studied the averaged flow field and the instantaneous flow field structure in the Santiago & Dutton experiment [18], and demonstrated that the mixing in the upstream windward shear layer is mainly caused by Kelvin–Helmholtz (K-H) instability. Peterson & Candler [30] studied the supersonic transverse jet with the angle of 30° and 90° using RANS/LES methods and compared the difference in between the two flow fields.

Based on the previous LES validations and studies of the mixing and combustion of the supersonic transverse jet by Zhao et al. [31, 32], the objective of this further study is mainly focused on the influence of the reflected shock on mixing performance under different jet to cross-flow momentum flux ratios. This article is organized as follows: in Section 2, simplified description of JISCF combustor is presented. Subsequently, the details of LES method including the governing equations, numerical aspects and boundary conditions are briefly addressed in Section 3. In Section 4, the numerical results, which highlight the shock-enhanced mixing process and mechanism, are presented and discussed. Finally, the main conclusions drawn from the results and suggestions are summarized in Section 5.

2. Description of JISCF Combustor

The high-enthalpy hydrogen JISCF combustor, similar to the experimental setup at Stanford University [33], is numerically investigated in the present study. The side-view schematic of the chamber is shown in Fig. 1. Inlet height of the combustor is 23 mm. The compression ramp has a divergence angle of 10^{o} to generate a shock train. The injection orifice with a diameter of D = 2 mm is located at 70 mm downstream of the cross-flow inlet. The height of constant area section is 15 mm (h) in the normal y-direction with a width of 75 mm in the spanwise z-direction. The flow conditions of the incoming air stream and the hydrogen jet are given in Table 1. The incoming air freestream air has a high static temperature of Ta = 1200 K with a speed of 1908 m/s (Ma = 2.8). The jet-to-cross-flow momentum ratio *J*, defined as $J = \rho_j U_j^2 / \rho_\infty U_\infty^2$, is equal to 0.7, 2.11 and 4.0, respectively, in the present study. The total length L in the stream-wise (x-) direction of computational domain is 170mm including 35D upstream and 50D downstream of the injection orifice.

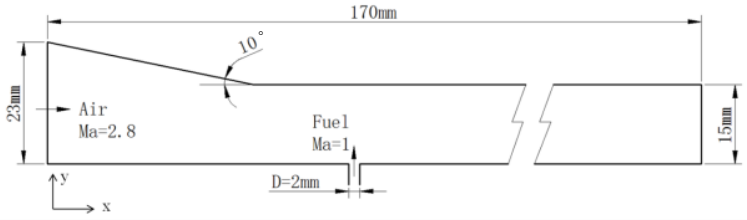

Fig. 1. Schematic of the combustor [32].

3. LES Governing Equations and Numerical Aspects

Filtering the instantaneous balance equations of mass, momentum, species mass fraction and total energy, the large-scale governing equations can be obtained [31],

$$\frac{\partial \bar{\rho}}{\partial t} + \frac{\partial \bar{\rho}\tilde{u}_j}{\partial x_j} = 0, \tag{3.1}$$

$$\frac{\partial \bar{\rho}\tilde{u}_i}{\partial t} + \frac{\partial \bar{\rho}\tilde{u}_i\tilde{u}_j}{\partial x_j} = -\frac{\partial \bar{p}}{\partial x_i} + \frac{\partial}{\partial x_j}\left(\bar{\tau}_{ij} - \tau_{ij}^{sgs}\right), \tag{3.2}$$

$$\frac{\partial \bar{\rho}\tilde{Y}_m}{\partial t} + \frac{\partial \bar{\rho}\tilde{u}_j\tilde{Y}_m}{\partial x_j} = \frac{\partial}{\partial x_j}\left[\bar{\rho}D\frac{\partial \tilde{Y}_m}{\partial x_j} - \tau_{\tilde{\phi}}^{sgs}\right] \quad (m = 1, \cdots, N), \tag{3.3}$$

$$\frac{\partial \bar{\rho}\tilde{E}}{\partial t} + \frac{\partial}{\partial x_j}\left[(\bar{\rho}\tilde{E} + p)\tilde{u}_j\right] = \frac{\partial}{\partial x_j}\left[\lambda\frac{\partial \tilde{T}}{\partial x_j} + \tilde{u}_j\bar{\tau}_{ij} - H^{sgs} - \sigma^{sgs}\right], \tag{3.4}$$

where $\bar{\rho}$ and $\bar{p}$ are filtered density and pressure. $\tilde{u}_{j(j=1,2,3)}$ is the filtered velocity component. The filtered viscous stress tensor $\bar{\tau}_{ij}$ is computed by using the filtered strain rate tensor $\tilde{S}_{ij}$. $\widetilde{Y_m}$ is the filtered mass fraction of species m and D is the molecular mass diffusivity. The molecular mass diffusivity is $D = \mu/\rho Sc$ [34, 35], where $\mu = \frac{A_s\sqrt{T}}{1+\frac{T_s}{T}}$ is the dynamic viscosity by using Sutherland's law and Sc is Schmidt number. $\tilde{E} = \tilde{e} + \frac{1}{2}\tilde{u}_j^2 + k^{sgs}$ is the filtered total energy. λ is the molecular thermal diffusivity, $\lambda = \mu C_p/Pr$, where laminar Prandtl number $Pr = 0.72$. The relation between pressure and temperature is assumed by the perfect gas state equation

$$\bar{P} = \bar{\rho}R(\tilde{Y}_m)\tilde{T}, \tag{3.4}$$

where $R(\tilde{Y}_m)$ is the mixture gas constant.

Various SGS closure models have been discussed in the literature [36] and the sensitivity study was carried by Toda et al. [37]. The sub-grid enthalpy flux H^{sgs} and the sub-grid viscous work σ^{sgs} in Eqs. (3.4) are closed as

$$H^{sgs} + \sigma^{sgs} = -\frac{\mu_t C_p}{Pr_t}\frac{\partial \tilde{T}}{\partial x_j} - \left(\mu_t + \mu\right)\frac{\partial k^{sgs}}{\partial x_j} + \tilde{u}_i\tau_{ij}^{sgs} \tag{3.5}$$

where the sub-grid kinetic energy and viscosity are modeled by $k^{sgs} = C_I\Delta^2\left(\overline{OP}\right)^2$ and $\mu_t = \bar{\rho}C_D\Delta^2\overline{OP}$ respectively. In the present study, the sub-grid scale terms are closed by the WALE (Wall-Adapting Local Eddy-viscosity) model [38]. Molecular transport properties of the species are defined by constant Prandtl and Schmidt numbers. The turbulent Prandtl number is set as $Pr_t = 0.9$ and the model coefficients C_I and C_D are determined by a dynamic procedure [37]. The sub-grid

scalar stresses are approximated using an eddy-diffusivity model, which is written as,

$$\tau_{\tilde{\phi}}^{sgs} = \left(\bar{\rho}\widetilde{u_j Y_m} - \bar{\rho}\tilde{u}_j\tilde{Y}_m\right) = -\bar{\rho}\widetilde{D_t}\nabla\tilde{\phi} \quad (3.7)$$

where $\widetilde{D}_t$ is the turbulent diffusivity modeled as $\bar{\rho}\widetilde{D}_t = \mu_t/Sc_t$, The turbulent Schmidt number is set as $Sc_t = 0.7$.

A new solver was developed and validated in our previous simulations [31, 32] based on the computational code of density solver in OpenFOAM [39], which was also used by other group to study supersonic mixing and combustion [40-44]. The convective fluxes are reconstructed using a second order (flux limiter-based) TVD scheme, while the viscous diffusion fluxes are implemented using the second order central differencing scheme. The discretization of species transport equation implemented in the code is the central-upwind scheme. The viscous effects are handled by solving the inviscid equation firstly, which is used as a predictor for the viscous solution. The time integration was performed by an explicit modified fourth order Runge-Kutta scheme with low storage requirement. The time-step is of the order of 10^{-9} with the courant number under 0.25. Each LES case is running for four flow-times (4L/U) to ensure the statistical stationary, where L is the axial length of computational zone and U is the mean velocity of air inlet. Time-averaging is performed for about six flow-times (6L/U).

For each case, the first set of grid is refined twice at the main fuel/air interaction locations using the post processing code of OpenFOAM to obtain a middle and a fine grid systems, detail of which can be found in table 1 as well as in Ref. [31]. Furthermore, according to Pope [45], the well-established turbulence resolution criterion, $Me = \frac{k_{sgs}}{k_{RES}+k_{sgs}} < 0.2$, characterizes a well-resolved LES in which at least 80% of the total turbulent kinetic energy is resolved, where k_{sgs} is the sub-grid turbulent kinetic energy and k_{RES} is the resolved turbulent kinetic energy. Fig. 2 shows the value of Me of the fine grid, which is computed by the data where hydrogen exists. As seen from the figure 3, the results show a good coherence comparing with the well-established turbulence resolution criterion, which means that the fine grid is able to predict the characteristics of the inertial subrange [45]. In order to ensure the accuracy of predictions, all the following simulations are performed by using the fine grid.

Table 1 mesh.

Cases	Coarse (million)	Middle (million)	Fine (million)
J = 0.71	4.8	7.5	14.3
J = 2.11	4.8	11.2	19.1
J = 4.00	4.8	12.1	26.2

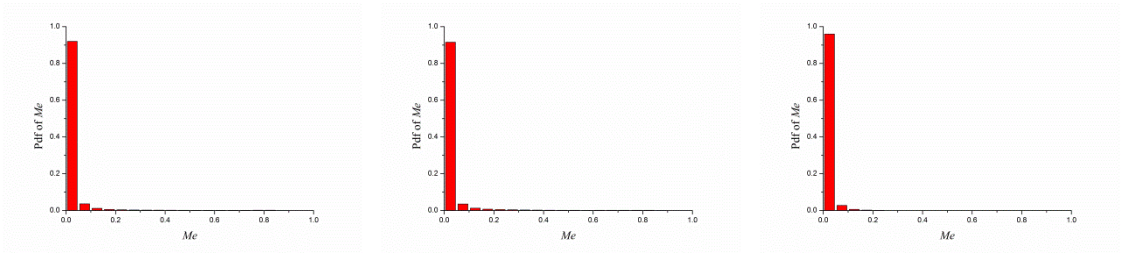

（a）*J*=0.71　　（b）*J*=2.11　　（c）*J*=4.00

Fig. 2. Distribution of the turbulence resolution criterion *Me* of the fine grid.

4. Results and Discussion

4.1 Effects of Reflected Shock on the Flow Fields

The previous studies of the non-reacting cases [31] and reacting case [32] of the high-enthalpy hydrogen JISCF combustor show that typical three-dimensional flow structures mainly include horseshoe vortex, counter rotating vortex pair, trailing counter rotating vortex pair, shear layer vortex and typical three-dimensional shock structures, such as Bow shock, Lambda shock, Mach disk and Barrel shock. Interactions between those complex shock structures and the flow structures can promote the mixing and increase the local temperature of gaseous in JISCF combustor. On the other hand, an oblique shock train is generated at the tip of the inlet compression ramp and reflected by the upper and lower walls.

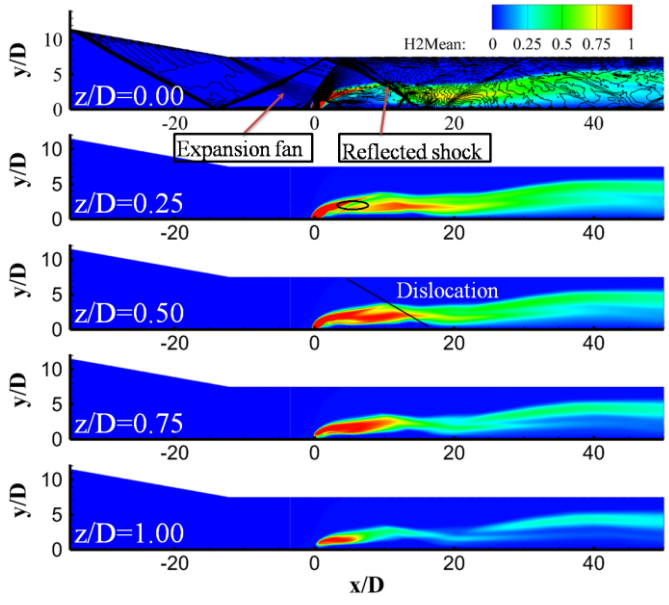

(a)

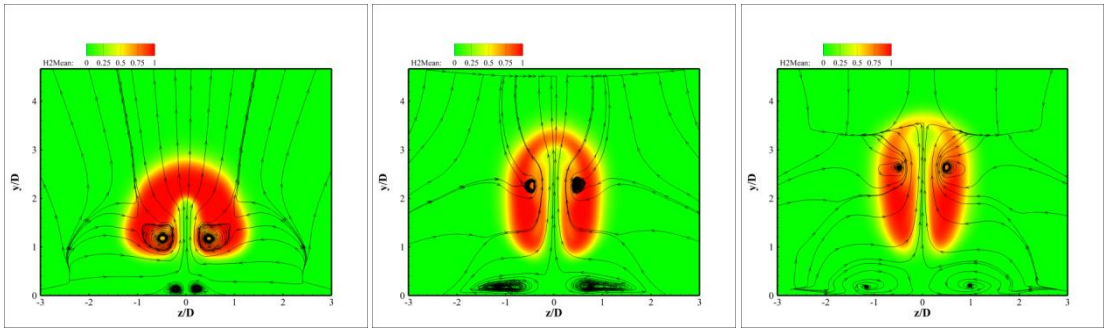

(b)

Fig. 3. (a): Mean Hydrogen Mass Fraction in Different Span-wise x-y Plane (z/D = 0, 0.25, 0.5, 0.75 & 1) and (b): Mean Hydrogen Mass Fraction, Contours and Streamlines at x/D = 4, 8 and 10 for J = 2.11.

Fig.3 shows the contours of the mean hydrogen mass fraction in five span-wise x-y planes, z/D = 0, 0.25, 0.5, 0.75 & 1, respectively. The instantaneous pressure contours in terms of the solid line in the midspan plane (z/D = 0) illustrates the expansion fans, the shocks and reflected shock waves. It can be found that the hydrogen mass fraction distribution exhibits a "dislocation" phenomenon along the reflected shock in all the five planes, which is mainly caused by the velocity deflection due to the reflected shocks. It is noteworthy that large-scale CVP structures (seen as in Fig. 3 (b)) lead to the interesting distribution shape of hydrogen mass fraction in span-wise planes, especially the region marked by an epllise in the plane z/D = 0.25, in which much more crossflow air flow is entrained.

The interactions between fuel jet plume and shock waves can enhance the mixing of the fuel jet with the surrounding air fluid, as noticed in ref [46]. Fig. 4 shows the mean flow field of the case J = 2.11 on the five cross-planes, x/D = 8, 9, 10, 11, 12 & 13, which further reflect the interaction between the shock and hydrogen jet plume. The first column is the result of the distribution of the numerical schlieren ($\|\nabla\bar{\rho}\|$), in which one can clearly observe the structures of shocks and that of the mixing layers due to the density difference between cross-flow air and hydrogen jet plume. The second row is the vorticity magnitude of average stream-wise vortex defined as $\omega_x = \partial v/\partial z - \partial w/\partial y$. And the third column is the velocity vector and distribution of the average hydrogen mass fraction. In addition, the position of the reflected oblique shock shown in the first column is marked by a solid line in the second column to better understand the interaction between the oblique shock and hydrogen jet plume. The outer moving shocks can be clearly observed in the first column, which is induced by the high-pressure zone between the jet plume and the bottom wall. Combined the first and third columns, this high-pressure zone produces a strong ascending velocity and drives air into the jet plume core to increase penetration of the jet plume boundary in the span wise direction, and the outer moving shocks move to the both sides with the increasing of the TCVP [47]. It should be noted that the thickness of the shock wave in the average field is relatively large, which can be mainly due to the unsteady characteristics of the shock wave in the flow field. With an increasing downstream distance (x/D), the CVP in the second column is being deformed to approach each other due to the moving down of the

reflected shock. The boundary layer in the TCVP region is strongly separated and two pairs of counter-rotating vortices are formed as shown in the second column. The distribution of the flow field can be clearly observed from the average velocity vector under the influence of the reflected oblique shock. Most of the velocity vector in the hydrogen jet plume are in the state of rising on the cross section due to the air entrainment by CVP when the oblique shock does not reach the surface of hydrogen jet plume at locations x/D = 8 and 9. At the same time on the upper side of the reflected oblique shock, the direction of the velocity in the cross-planes is downward due to the reflected oblique shock. On the cross-planes x/D=10, 11, 12 and 13, where the reflected oblique shock reaches the jet plume surface and passes through the jet plume, the direction of entrained air driven by the ascending velocity is changed near the reflected oblique shock due to the strong discontinuous of the shocks. A region dominated by the cross-flow air is formed in the jet plume, and thus promotes the mixing of the fuel jet and air. The downward flow will then drive the air into the hydrogen jet plume to further promote the mixing process. In fact, the R-M instability occurs when the shock waves interact with the interfaces of two different fluid [48, 49]. Moreover, the boundary layer of the hydrogen jet plume in the span-wise is widened due to the interaction of shocks and the hydrogen jet plume.

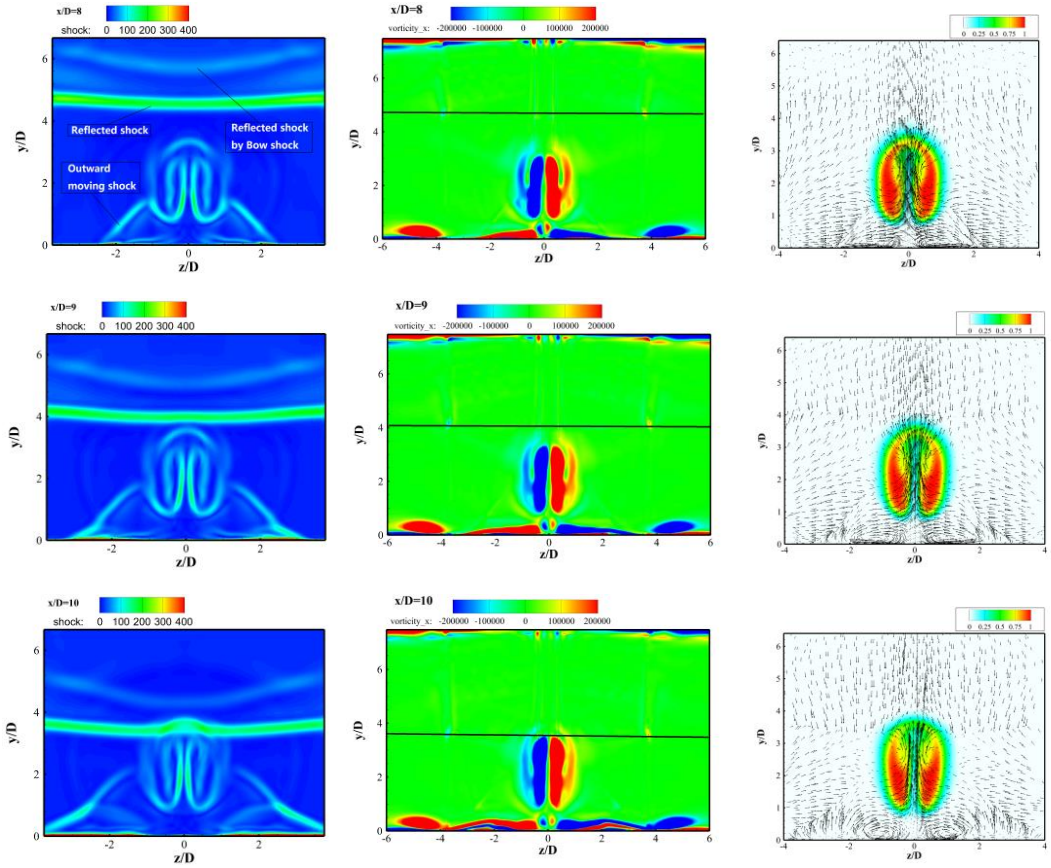

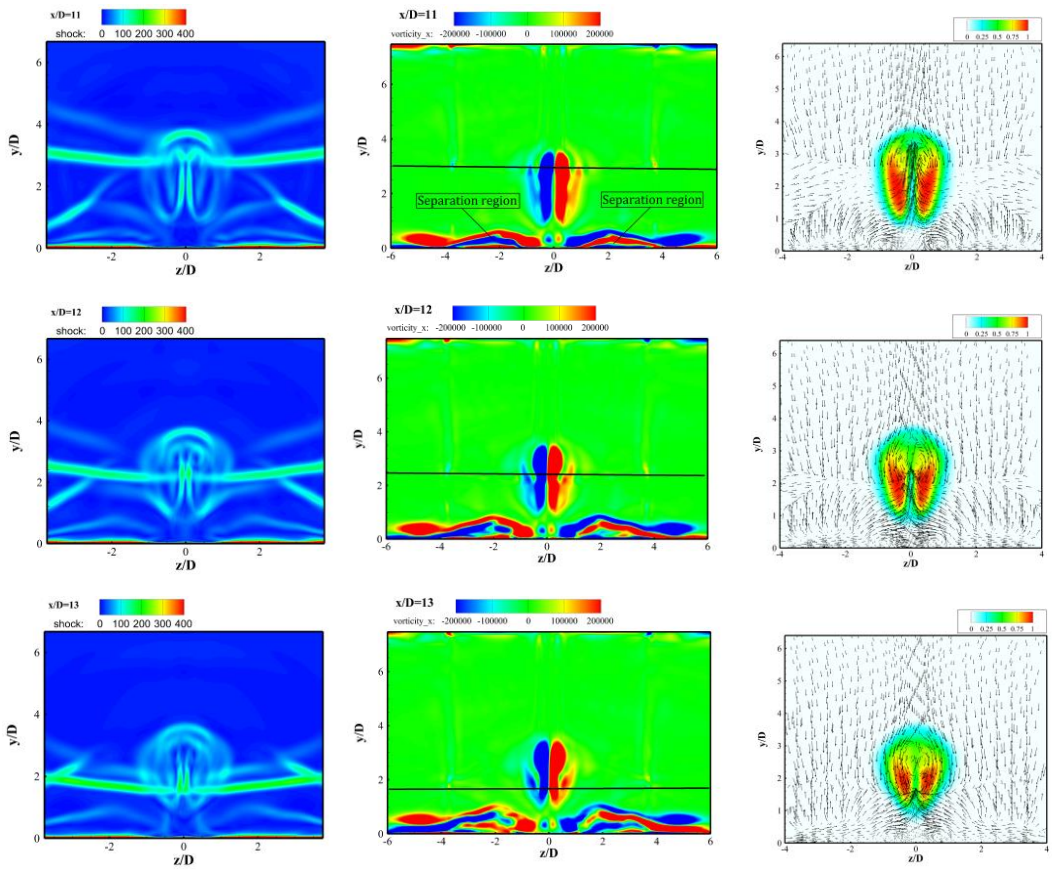

Fig. 4. Information of mean flow field at different cross-planes (x/D = 8, 9, 10, 11, 12 &13) of J = 2.11.

Since the penetration depth in the span-wise direction is particularly important for the studied JISCF combustor due to the upper wall, two length scales are used to characterize the hydrogen jet penetration depth, the distance between the vertex core of CVP in the span-wise (z) direction and the distance from the CVP core to the bottom wall in a cross section [50]. Fig. 5 illustrates the non-dimensional jet penetration depth, y/D and z/D, which represents half of the distance between the vertex core of CVP in the span-wise (z) direction, along the streamwise direction of the three cases. The penetration depth y/D is found to be high with the increasing of the jet to cross-flow momentum flux ratio J in the near field (x/D<12), which agrees well with that in Wang et al. [50]. The penetration depth z/D of the cases J = 2.11 and 4.00 will not increase downstream of the location x/D = 12 due to the influence of the upper wall. In the relative far field, 8 < x/D < 15, there is little change on the penetration depth in the span-wise direction for J = 4.11; while for J = 0.71 and 2.11, the penetration depth z/D stays near the same between x/D of 3 and 20. In the near field, there is a peak value of the penetration depth z/D for each case due to the interaction of the sonic hydrogen jet and the supersonic cross-flow. In addition, due to the interaction between the reflected shock, the jet plume and the bottom wall, the penetration depth z/D is found to increase further downstream of location at x/D = 20. Therefore, the reflected shock can increase the distance between the core positions of counter-rotating vortex pair, which enables more mainstream air into the fuel jet plume.

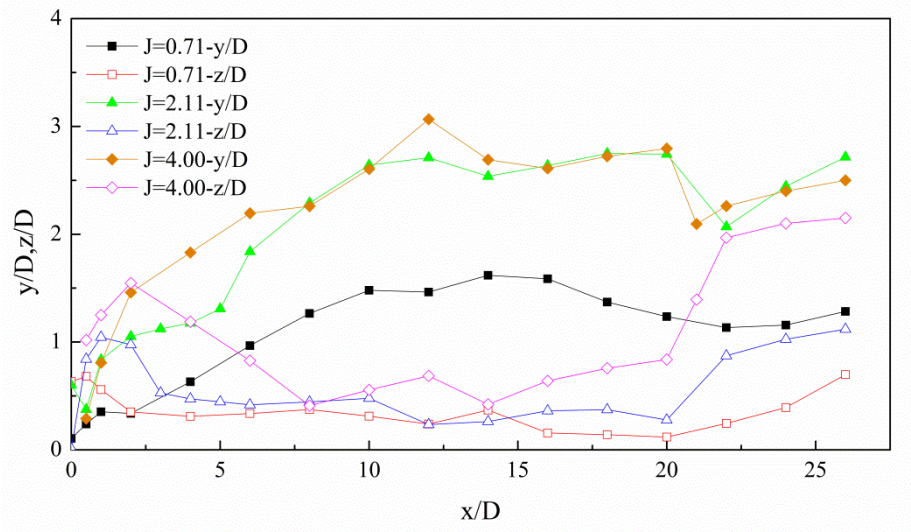

Fig. 5. Penetration in the span-wise and normal directions characterized by the core position of the CVP.

4.2 Vorticity analysis

It is generally believed that stream-wise vortex can help promoting the entrainment and mixing process of the fuel and incoming air in a scramjet combustion chamber [51-53]. The circulation of stream-wise vortex of mean flow field in a cross section is defined as follows [54]:

$$\tau(x) = \iint_{yz} \left| \frac{\partial v}{\partial z} - \frac{\partial w}{\partial y} \right| \rho u dy dz, \tag{4.6}$$

where u, v and w are the mean velocity components in the stream-wise, wall normal and span-wise directions respectively. Fig. 6(a) shows the circulation τ versues x/D of the three cases. The circulation τ is small upstream of the fuel jet orifice for all the three cases, which is related to the horseshoe vortex dominated by the span-wise vortex strength. The sonic jet encounters the supersonic cross-flow in the near field where the complex vortex structures, such as the hovering vortex, CVP and vortex generated by the baroclinic torque[55], are produced, and resulting in the first peak marked as P1 at about x/D=1.5. The larger jet to cross-flow momentum flux ratio *J*, the larger τ, which indicates that increasing the ratio *J* can strengthen the stream-wise vortex downstream the fuel jet orifice leading to the promotion of the air entrainment and the mixing process [51, 52]. This may be due to the higher baroclinic vortices generated by the higher jet to cross-flow momentum flux ratio [56, 57]. In addition, there are multiple peaks of the circulation τ for all the three cases shown in Fig. 6(a). The peak marked as P2 is associated with shocks after the Mach disk, which is significantly affected by the ratio *J*. However, it should be noted that P2 was not found for the case J=0.71 due to the weak Mach disk under lower *J*. The peak marked as P3 is linked to the reflected oblique shock wave marked as R1 shown in Fig. 6(b). Although P3 is not obvious for cases J= 0.71 and 2.11, the circulations of the stream-wise vortex are enhanced. The peak marked as P4（where the position of P4 for case *J*=0.71 is a little downstream of the similar position for the other two cases due to the weaker bow shock as seen in

Fig. 6(b) of the circulation of the stream-wise vortex is at about x/D = 20, where the reflected shock (R2 shown in Fig. 6(b)) interacts with the fuel jet plume and the bottom wall.

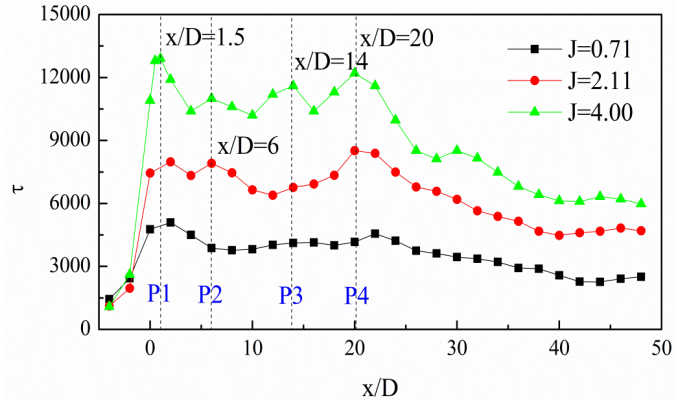

(a) Evolution of the averaged circulation of the stream-wise vortex τ versues x/D.

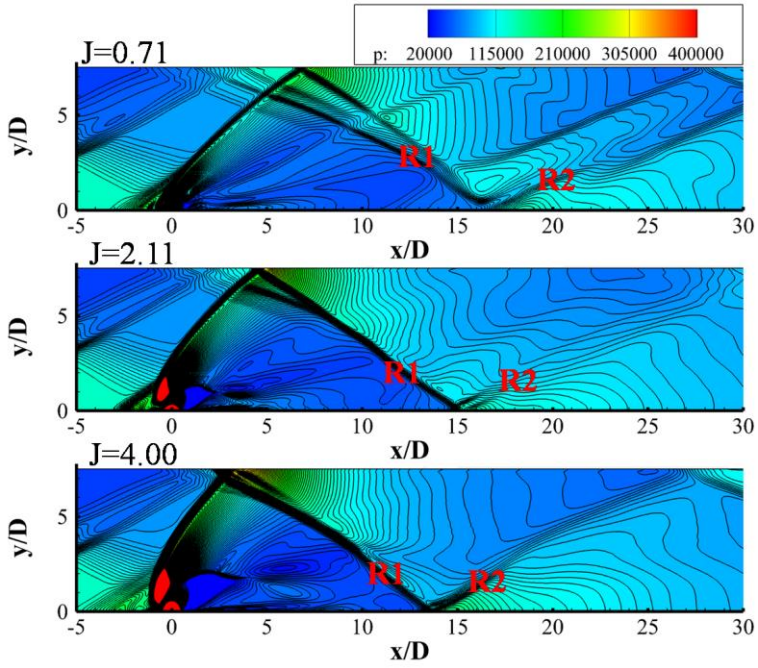

(b) Mean pressure distributions and contours in the central plane (z/D = 0).

Fig. 6. Evolution of the averaged circulation of the stream-wise vortex (a) and mean pressure distributions and contours in the central plane (z/D = 0) (b).

The vorticity transport equation is expressed as [58]:

$$\underbrace{\frac{\partial \boldsymbol{\omega}}{\partial t}}_{1} = \underbrace{-(\mathbf{v}\cdot\nabla)\boldsymbol{\omega}}_{2} + \underbrace{(\boldsymbol{\omega}\cdot\nabla)\mathbf{v}}_{3} + \underbrace{\left(-\boldsymbol{\omega}(\nabla\cdot\mathbf{v})\right)}_{4} + \underbrace{\frac{1}{\rho^2}\nabla\rho\times\nabla p}_{5} + \underbrace{\nu\nabla^2\boldsymbol{\omega}}_{6}, \qquad (4.7)$$

where, the terms from 2 to 6 on the right hand represent the inertial convective, vortex stretching, dilatational (or compressible), baroclinic and diffusion terms, respectively. It can be found that the vortex stretching and baroclinic terms not only change the magnitude but also the direction of the vorticity. On the other hand, the dilatational and baroclinic terms have significant effects on flow

structures in the supersonic flow.

The contours of vorticity magnitude in the central plane (z/D = 0) of the three cases are shown in Fig. 7. The unit of vorticity is s^{-1}, and the order of its magnitude is 10^7 Hz, so the mixing time should be 10^{-7} s. There exist strong vortex structures in the upstream recirculation zone of the jet nozzle and in the upwind and leeward jet shear layers.

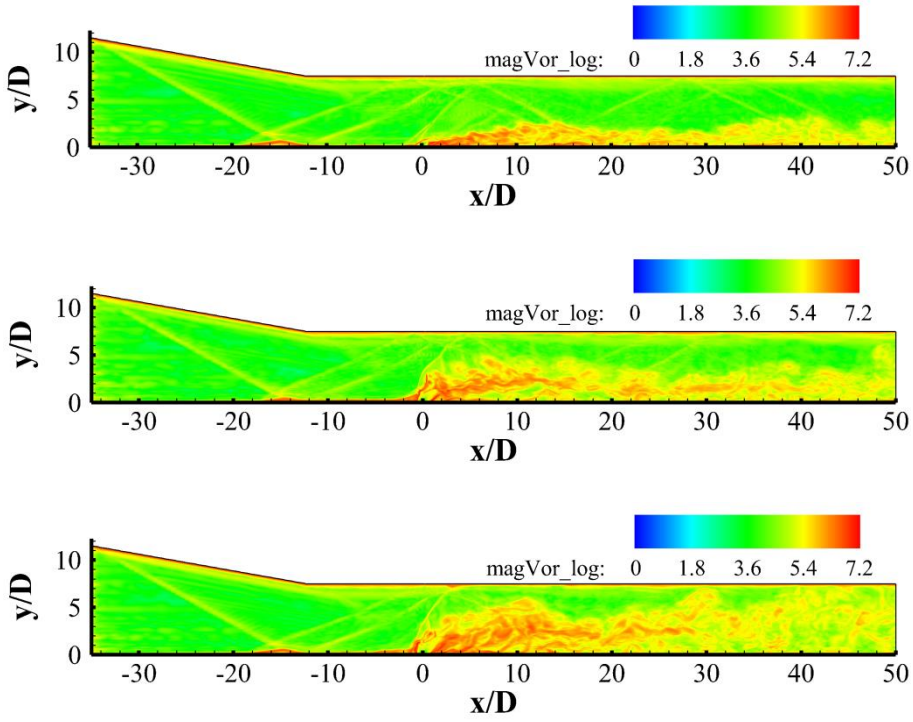

Fig. 7. Vorticity distributions in the central plane (z/D = 0) with *J* = 0.71, 2.11 & 4.0 from top to bottom.

To strengthen the fuel-oxidant mixing in the scramjet combustor, some researchers [59, 60& 61] proposed the concept of shock-induced vorticity. A simple method for generating the stream-wise vortex is to induce the baroclinic term (5) by means of shock waves. The mechanism of the vorticity generation by the baroclinic term can be simply expressed by the vorticity transport equation:

$$\rho \frac{D}{Dt}\left(\frac{\boldsymbol{\omega}}{\rho}\right) = \frac{1}{\rho^2}\nabla\rho \times \nabla p \,. \tag{4.3}$$

Vorticity is generated when the pressure gradient is not parallel to the density gradient. Considering the existence of a series of reflected shocks in the present JISCF combustor, the effects of baroclinic term are much more important on mixing in supersonic combustion [62].

Fig. 8 depicts the distributions of the magnitude of baroclinic term ($\log_{10}\left|\frac{1}{\rho^2}\nabla\rho \times \nabla p\right|$) in the central plane (z/D = 0) of the three-different jet to cross-flow momentum flux ratios. There are two regions with the larger magnitude of baroclinic term: the windward side shear layer just downstream the bow shock and the one just downstream the junction of the oblique shock waves and the fuel jet

plume. The fluid is compressed with a high-pressure gradient ∇p when passing through the oblique shock. The hydrogen jet and the supersonic air flow have a large density difference which leads to a high density gradient $\nabla \rho$ at the shear layer. Fig. 9(a) shows the magnitude of baroclinic term $\left|\frac{1}{\rho^2}\nabla\rho \times \nabla p\right|$ versues y/D at different stream-wise positions (x/D = 10, 11, 12 & 13) in the central plane (z/D = 0). High peak magnitude of baroclinic term is different for each case and is located in the place where the oblique shock interacts with jet plume. It is further proved that the baroclinic term, due to the interaction between the oblique shock and the jet plume, has a significant effect on the vorticity generation. Fig. 9(b) provides the distributions of the baroclinic term along the stream-wise direction at different normal positions (y/D = 0.25, 0.5, 1 & 2) in the central plane (z/D = 0). The baroclinic term in the shear layer after the bow shock is significantly higher than that in the oblique shock and jet plume interaction regions. Moreover, there also exists high baroclinic term on leeward sides of the jet in the downstream due to the outward moving shock.

The normalized baroclinic source term are defined as [63]:

$$BS = \frac{1}{\rho_\infty p_\infty}\iint_{yz} |\nabla\rho \times \nabla p| dydz, \tag{4.4}$$

where ρ_∞ and p_∞ are the cross-flow inlet density and pressure. Fig. 10 shows the normalized baroclinic source BS of the mean flow field in the y–z plane. It can be found that the increase of the average circulation of the stream-wise vortex arises after the increase of baroclinic source in conjunction with Fig. 6(a). The highest circulation in the near field is due to the highest intensity of baroclinic source. The second distinguishable peak noted as P4 of the circulation of the stream-wise vortex at about x/D = 20 is due to the baroclinic torque just before x/D =20, as seen in Fig. 10. In addition, a peak baroclinic source is found at x/D = 12, after which a peak of circulation of stream-wise vortex is found at x/D = 14 for J = 4.00, as seen in Fig. 6(a). Studies of Lee et al. [57] suggested that there are time delays between the changes of baroclinic source and the changes of vortex circulation. Hence, complex vortex structures generated by the interaction between oblique shock and fuel jet plume in the supersonic combustion chamber are due to the shock-induced baroclinic torque.

According to the vorticity transport equation, the dilatational term (4) also has significant effect on the vorticity generation in addition to the baroclinic term in compressible flow. There is relatively high value at the interface of the fuel jet plume and the supersonic incoming air flow in the near field. Thus, the dilatational term $-\boldsymbol{\omega}\left(\nabla\cdot\mathbf{v}\right)$ can promote vorticity generation and mixing process. Fig. 11 illustrates the distributions of the dilatational term ($\log_{10}\left|-\boldsymbol{\omega}\left(\nabla\cdot\mathbf{v}\right)\right|$) in the central plane z/D = 0 of the three jet to cross-flow momentum flux ratios. Note that the intensity of the dilatational term after the shock wave is strengthened; and the dilatational term caused by these shock waves can promote the generation of vortices and the mixing process of fuel and oxidant. There are highly baroclinic term and

dilatational term in the leeward side of the jet plume and leeward side of the shear layer. The two main items in the vorticity equation are mainly caused by the Mach disk, barrel shock and wake shock, resulting in a high vorticity generation in the leeward side of the jet plume and leeward side shear layer as shown in Fig. 7.

The vorticity stretching term (3) is relatively large in the subsonic recirculation zone, that the vorticity produced by the baroclinic term and diffusion term is transported to upstream region. The formation of the horseshoe vortex is relevant to this transportation. The viscous-related vorticity source term is on the order of magnitude smaller than those terms mentioned above [64].

In general, the compressibility, vortex stretching and baroclinic terms are all important, and with the same order of magnitude in the supersonic flow. They all affect the vorticity generation in the same way, however at different locations for the fuel and oxidant mixing process.

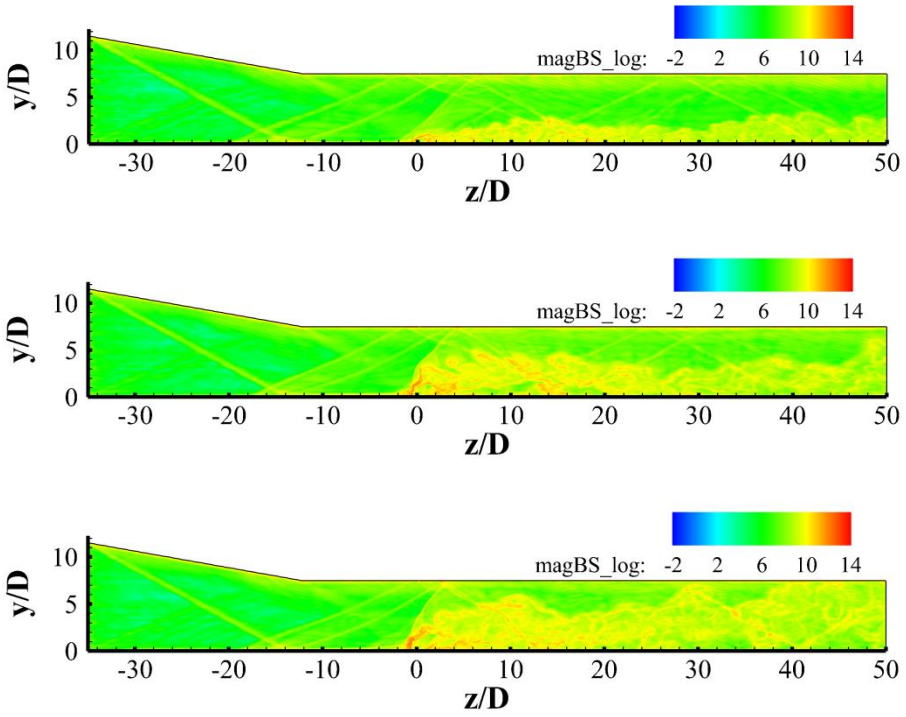

Fig. 8. Distributions of the baroclinic term ($\log_{10}\left|\frac{1}{\rho^2}\nabla\rho\times\nabla p\right|$) in the central plane (z/D = 0) with J = 0.71, 2.11 & 4.0.

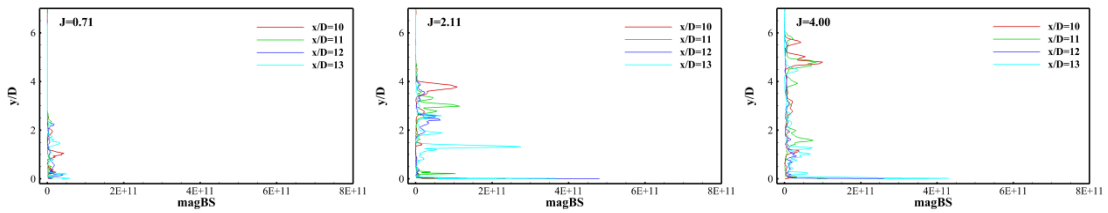

(a)

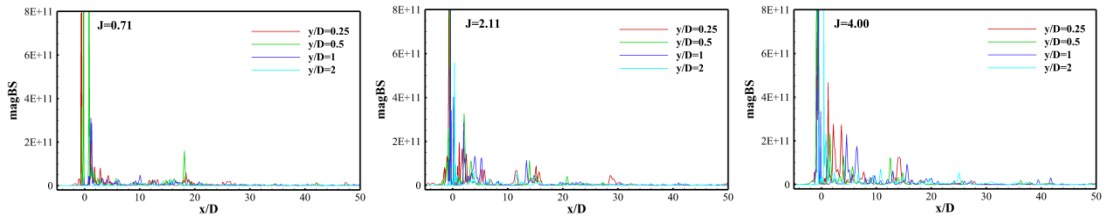

(b)

Fig. 9. The distributions of baroclinic term, (a) along the normal direction at different stream-wise positions and (b) along the stream-wise direction at different normal positions in the central plane (z/D = 0).

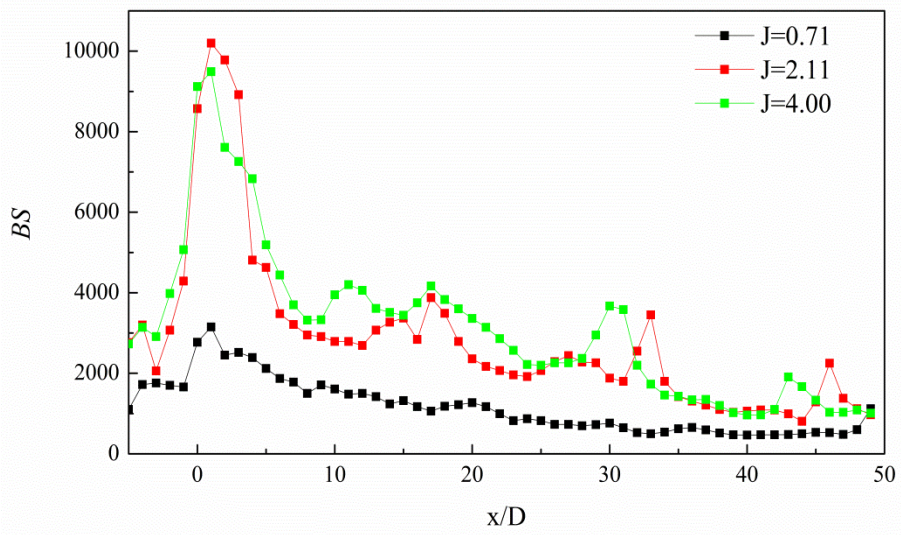

Fig. 10. The normalized baroclinic source of the mean flow field in y–z plane.

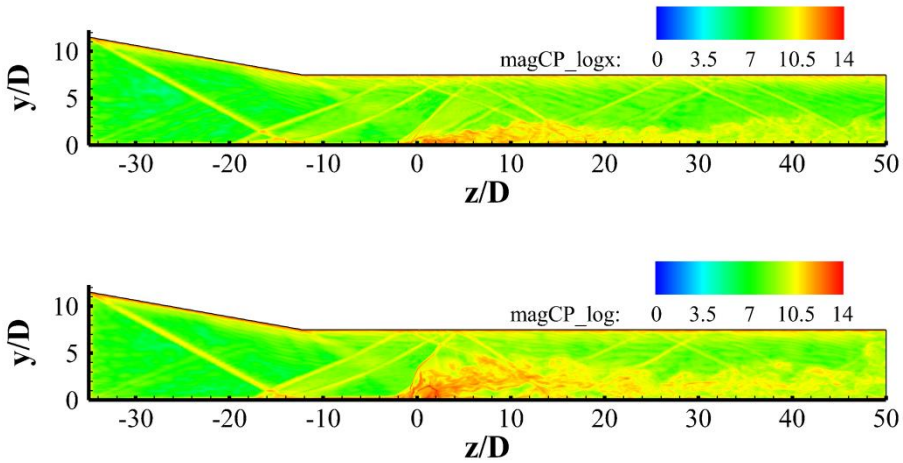

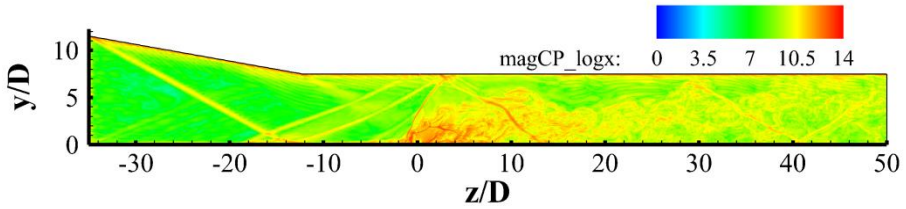

Fig. 11. The dilatational term ($\log_{10}|-\omega(\nabla \cdot v)|$) distributions in the central plane (z/D = 0) with J = 0.71, 2.11 & 4.0.

4.3 Probability Density Function of Mixture Fraction

Considering the spatial-temporal quantity, Fig. 12(a) provides the probability density function (PDF) of mixture fraction in different streamwise planes. All curves demonstrate a large portion of unmixed cross-flow air at Z = 0 and little unmixed hydrogen jet at Z = 1, where the dotted line represents the stoichiometric mixture corresponding to the mixture fraction Z_{st} =0.0283. In the near field x/D = 4, the hydrogen jet core starts mixing at the lower momentum flux ratio J = 0.71; while for other two momentum flux ratios the hydrogen jet cores are still unmixed. It is very important for fuel jet mixing that the cross-flow air is entrained into the fuel jet plume with the influence of CVP. Although the larger CVP is observed downstream of the jet in the higher jet to cross-flow momentum flux ratio, interaction between the wall and the CVP is much stronger in the relatively low J and the entrainment of cross-flow air is more intense. It can well be seen that both the shape and peak position of the distributions are influenced by J. Except from that, the PDF of hydrogen fraction is higher in the near filed but lower in the far field for J = 4.00, which indicates that the mixing is not only influenced by the size of CVP but also the interaction between the wall and CVP.

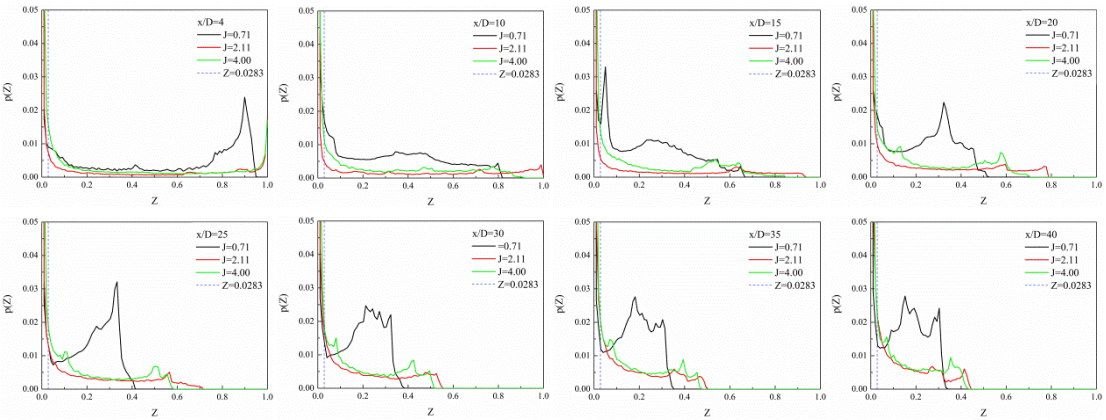

(a)

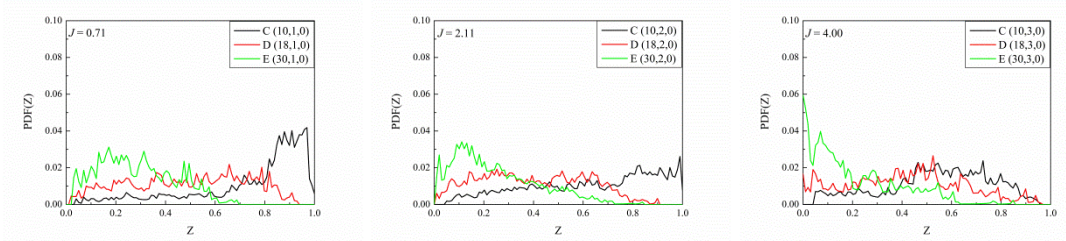

(b)

Fig. 12. Probability density function of mixture fraction in the stream-wise plane (a) and at three specific locations for each case (b).

In order to study the mixing characteristics at a particular location, Fig. 12(b) shows the probability density function of mixture fraction at three specific locations. The three detection points C、D and E are all in central plane z/D=0, with coordinate values x/D = 10, 18 & 30, respectively for all the three ratios *J*, while coordinate value y/D are set to be 1, 2, 3 for *J* = 0.71, 2.11, 4.00 for the three detection points respectively, corresponding to the region before oblique shock wave, after oblique shock wave and in the far field. All data records start from the statistical state, about three flow-through time (L/U_c). It can be found that the mixture fraction is close to Z = 1 at the position of x/D =10, indicating that the evolution of jet is dominated by large scale motion before the oblique shock wave. In the position of x/D = 18 after the oblique shock, the probability density distributions of the sample points are relatively uniform. The multi-scale inhomogeneity of the jet plume indicates the unsteady characteristics of the large-scale structures and the broken process while passing though the oblique shock wave. The coexistence and interactions of multi-scale structures promote the mixing process of the jet plume and the surrounding air flow. At the far field x/D = 30, the probability density distributions of the mixture fraction are mainly concentrated near Z = 0, indicating uniformity and small scale of mixing in the far field.

5. Conclusion

In the present work, large-eddy simulation of shock-enhanced mixing in a transverse hydrogen injection combustor with an inlet compression ramp is conducted to investigate the mixing process and mechanism. The main conclusions are summarized as follows.

Effects of a shock train induced by the inlet compression ramp have a significant impact on the mixing process. The strong discontinuous of the oblique shock wave changes the direction of the velocity in the cross-planes flow and a region dominated by the cross-flow is created in the jet plume, which promotes the mixing of the fuel jet and air.

The results of vorticity analysis demonstrates that the shock-induced baroclinic torque plays an important role on the generation of the vorticity in the near field of the jets and the place where the reflected shock interacting with the jet plume.

The probability density function of the mixture fraction suggests that the coexistence and interaction of the multi-scale structures, after the oblique shock wave, promote the mixing process of the jet plume and the surrounding air flow.

Acknowledgment

This work is supported by the National Natural Science Foundation of China (Grant No. 91441117 and Grant No. 51576182). The numerical simulations in this paper have been performed on

the supercomputers in the Supercomputing Center, University of Science and Technology of China.

References

[1] Curran E T. Scramjet engines: the first forty years[J]. Journal of Propulsion and Power, 2001, 17(6): 1138-1148.

[2] Huang W. Transverse jet in supersonic crossflows[J]. Aerospace Science and Technology, 2016, 50: 183-195.

[3] Karagozian A R. Transverse jets and their control[J]. Progress in Energy and Combustion Science, 2010, 36(5): 531-553.

[4] Mahesh K. The interaction of jets with crossflow[J]. Annual review of fluid mechanics, 2013, 45: 379-407.

[5] Liang C, Sun M, Liu Y, et al. Shock wave structures in the wake of sonic transverse jet into a supersonic crossflow[J]. Acta Astronautica, 2018, 148: 12-21.

[6] Zhao Y, Liang J, Zhao Y. Vortex structure and breakup mechanism of gaseous jet in supersonic crossflow with laminar boundary layer[J]. Acta Astronautica, 2016, 128: 140-146.

[7] Mai, T., Sakimitsu, Y., Nakamura, H., Ogami, Y., Kudo, T., & Kobayashi, H. Effect of the incident shock wave interacting with transversal jet flow on the mixing and combustion[J]. Proceedings of the Combustion Institute, 2011, 33(2): 2335-2342.

[8] Margason R J. Fifty years of jet in cross flow research[C]//In AGARD, Computational and Experimental Assessment of Jets in Cross Flow 41 p (SEE N94-28003 07-34). 1993, 1.

[9] Li LQ, Huang W, Yan L, Li SB. Parametric effect on the mixing of the combination of a hydrogen porthole with an air porthole in transverse gaseous injection flow fields [J]. Acta Astronautica. 2017 Oct 1;139:435-48.

[10] Wang Y, Wang Z, Sun M, Wang H, Cai Z. Effects of fueling distance on combustion stabilization modes in a cavity-based scramjet combustor [J]. Acta Astronautica. 2019 Feb 1;155:23-32.

[11] Liu C, Zhao Y, Wang Z, et al. Dynamics and mixing mechanism of transverse jet injection into a supersonic combustor with cavity flameholder[J]. Acta Astronautica, 2017, 136: 90-100.

[12] Seiner J M, Dash S M & Kenzakowski D C. Historical survey on enhanced mixing in scramjet engines[J]. Journal of Propulsion and Power, 2001, 17(6): 1273-1286.

[13] Yang J, Kubota T & Zukoski E E. Applications of shock-induced mixing to supersonic combustion[J]. AIAA journal, 1993, 31(5): 854-862.

[14] Ratner, A., Driscoll, J. F., Huh, H., & Bryant, R. A. Combustion efficiencies of supersonic flames[J]. Journal of Propulsion and Power, 2001, 17(2): 301-307.

[15] Rubins P M & Bauer R C. Review of shock-induced supersonic combustion research and

hypersonic applications[J]. Journal of Propulsion and Power, 1994, 10(5): 593-601.

[16] Nakamura, H., Sato, N., Ishida, S., Ogami, Y., & Kobayashi, H. A Study of Interaction between Shock Wave and Cross-Flow Jet Using Particle Tracking Velocimetry[J]. Transactions of The Japan Society for Aeronautical and Space Sciences, 2009, 52(176): 81-88.

[17] Aso, S., Okuyama, S., Kawai, M & Ando, Y (1991). Experimental study on mixing phenomena in supersonic flows with slot injection. *AIAA paper*, *16*, 1991.

[18] Santiago J G & Dutton J C. Velocity measurements of a jet injected into a supersonic crossflow [J]. *Journal of Propulsion and Power*, 1997, 13(2): 264-273.

[19] Gruber, M. R., Nejadt, A. S., Chen, T. H., & Dutton, J. C. Mixing and penetration studies of sonic jets in a Mach 2 freestream[J]. Journal of Propulsion and Power, 1995, 11(2): 315-323.

[20] Gruber, M. R., Nejad, A. S., Chen, T. H., & Dutton, J. C. Compressibility effects in supersonic transverse injection flowfields [J].*Physics of Fluids (1994-present)*, 1997, 9(5): 1448-1461.

[21] Gamba M & Mungal M G. Ignition, flame structure and near-wall burning in transverse hydrogen jets in supersonic crossflow[J]. Journal of Fluid Mechanics, 2015, 780: 226-273.

[22] Kobayashi, K., W. Bowersox, R. D., Srinivasan, R., Tichenor, N. R., Carter, C. D., & Ryan, M. D. Experimental and numerical studies of diamond-shaped injector in a supersonic flow[J]. Journal of Propulsion and Power, 2010, 26(2): 373-376.

[23] Chaudhuri, A., Hadjadj, A., Chinnayya, A., & Palerm, S. Numerical study of compressible mixing layers using high-order WENO schemes[J]. Journal of Scientific Computing, 2011, 47(2): 170-197.

[24] Huete, C., Sánchez, A. L., Williams, F. A., & Urzay, J. Diffusion-flame ignition by shock-wave impingement on a supersonic mixing layer[J]. Journal of Fluid Mechanics, 2015, 784: 74-108.

[25] Huete, C., Urzay, J., Sánchez, A. L., & Williams, F. A. Weak-shock interactions with transonic laminar mixing layers of fuels for high-speed propulsion[J]. AIAA Journal, 2016, 54(3): 966-979.

[26] Huang, W., Wang, Z. G., Wu, J. P., & Li, S. B. Numerical prediction on the interaction between the incident shock wave and the transverse slot injection in supersonic flows[J]. Aerospace Science and Technology, 2013, 28(1): 91-99.

[27] Ben-Yakar A, Mungal M G & Hanson R K. Time evolution and mixing characteristics of hydrogen and ethylene transverse jets in supersonic crossflows[J]. *Physics of Fluids* (1994-present), 2006, 18(2): 026101.

[28] Chai X, Iyer P S & Mahesh K. Numerical study of high speed jets in crossflow[J]. Journal of Fluid Mechanics, 2015, 785: 152-188.

[29] Rana Z A, Thornber B & Drikakis D. Transverse jet injection into a supersonic turbulent

cross-flow[J]. Physics of Fluids (1994-present), 2011, 23(4): 046103.

[30] Peterson D M & Candler G V. Simulations of Mixing for Normal and Low-Angled Injection into a Supersonic Crossflow[J]. AIAA journal, 2011, 49(12): 2792-2804.

[31] Zhao, M., Ye, T., Cao, C., Zhou, T., & Zhu, M. Study of sonic injection from circular injector into a supersonic cross-flow using large eddy simulation[J]. International journal of hydrogen energy, 2016, 41(39): 17657-17669.

[32] Zhao, M., Zhou, T., Ye, T., Zhu, M., & Zhang, H. Large eddy simulation of reacting flow in a hydrogen jet into supersonic cross-flow combustor with an inlet compression ramp[J]. International Journal of Hydrogen Energy, 2017, 42(26): 16782-16792. [33] Gamba, M., Miller, V., Mungal, M. G., & Hanson, R. Ignition and flame structure in a compact inlet/scramjet combustor model[C]//17th AIAA International Space Planes and Hypersonic Systems and Technologies Conference. 2011: 2366.

[34] Heidari A, Wen J X. Numerical simulation of flame acceleration and deflagration to detonation transition in hydrogen-air mixture[J]. International Journal of Hydrogen Energy, 2014, 39(36): 21317-21327.

[35] Maragkos G, Rauwoens P, Fauconnier D, et al. Large eddy simulations of differential molecular diffusion in non-reacting turbulent jets of H2/CO2 mixing with air[J]. Physics of Fluids (1994-present), 2014, 26(2): 025102.

[36] Garnier E, Adams N, Sagaut P. Large eddy simulation for compressible flows[M]. Springer Science & Business Media, 2009.

[37] Toda H B, Truffin K, Nicoud F. Is the dynamic procedure appropriate for all SGS model[C]//V European Conference on Computational Fluid Dynamics, ECCOMAS, Lisbon, Portugal. 2010: 14-17.

[38] Nicoud F, Ducros F. Subgrid-scale stress modelling based on the square of the velocity gradient tensor[J]. Flow, turbulence and Combustion, 1999, 62(3): 183-200.

[39] Jasak H. Error analysis and estimation for the finite volume method with applications to fluid flows[J]. 1996.

[40] Cai, Z., Liu, X., Gong, C., Sun, M., Wang, Z., and Bai, X.-S. "Large Eddy Simulation of the fuel transport and mixing process in a scramjet combustor with rearwall-expansion cavity," Acta Astronautica Vol. 126, 2016, pp. 375-381.

[41] Wang, Z., Cai, Z., Sun, M., Wang, H., and Zhang, Y. "Large Eddy Simulation of the flame stabilization process in a scramjet combustor with rearwall-expansion cavity," International Journal of Hydrogen Energy Vol. 41, 2016, pp. 19278-19288.

[42] Cai, Z., Zhu, J., Sun, M., ZhenguoWang, and Bai, X.-S. "Laser-Induced Plasma Ignition in a Cavity-Based Scramjet Combustor," AIAA Journal Vol. 56, No. 12, 2018, pp. 4884-4892.

[43] Cai, Z., Zhu, J., Sun, M., and Wang, Z. "Effect of cavity fueling schemes on the laser-induced

plasma ignition process in a scramjet combustor," Aerospace Science and Technology Vol. 78, 2018, pp. 197-204.

[44] Cai, Z., Wang, Z., Sun, M., and Bai, X.-S. "Effect of combustor geometry and fuel injection scheme on the combustion process in a supersonic flow," Acta Astronautica Vol. 129, 2016, pp. 44-51.

[45] Pope S B. Turbulent flows[J]. 2001.

[46] Andreopoulos Y, Agui J H & Briassulis G. Shock wave turbulence interactions. *Annu Rev Fluid Mech*, 2000, 32: 309-345

[47] Génin F & Menon S. Dynamics of sonic jet injection into supersonic crossflow[J]. Journal of Turbulence, 2010 (11): N4.

[48] Nordin-Bates, K., Fureby, C., Karl, S., & Hannemann, K. Understanding scramjet combustion using LES of the HyShot II combustor[J]. Proceedings of the Combustion Institute, 2017, 36(2): 2893-2900.

[49] Khokhlov A M, Oran E S & Thomas G O. Numerical simulation of deflagration-to-detonation transition: the role of shock–flame interactions in turbulent flames[J]. Combustion and Flame, 1999, 117(1): 323-339.

[50] Wang G L, Chen L W & Lu X Y. Effects of the injector geometry on a sonic jet into a supersonic crossflow[J]. Science China Physics, Mechanics and Astronomy, 2013, 56(2): 366-377.

[51] Lee S H. Characteristics of dual transverse injection in scramjet combustor, Part 1: Mixing[J]. Journal of Propulsion and Power, 2006, 22(5): 1012-1019.

[52] Ingenito A & Bruno C. Physics and regimes of supersonic combustion[J]. AIAA journal, 2010, 48(3): 515-525.

[53] Gerlinger P, Stoll P, Kindler M, Schneider F & Aigner M. Numerical investigation of mixing and combustion enhancement in supersonic combustors by strut induced streamwise vorticity[J]. Aerospace Science and Technology, 2008, 12(2): 159-168.

[54] Lee S H & Mitani T. Mixing augmentation of transverse injection in scramjet combustor[J]. Journal of propulsion and power, 2003, 19(1): 115-124.

[55] Ben-Yakar A. Experimental investigation of mixing and ignition of transverse jets in supersonic crossflows [D]. *Palo Alto: Stanford University*, 2000.

[56] Waitz I A, Marble F E & Zukoski E E. Investigation of a contoured wall injector for hypervelocity mixing augmentation[J]. AIAA journal, 1993, 31(6): 1014-1021

[57] Lee S H, Jeung I S & Yoon Y. Computational investigation of shock-enhanced mixing and combustion[J]. AIAA journal, 1997, 35(12): 1813-1820.

[58] Li X, Yao W & Fan X. Large-Eddy Simulation of Time Evolution and Instability of Highly Underexpanded Sonic Jets[J]. AIAA Journal, 2016: 1.

[59] Billig F S. Research on supersonic combustion[J]. Journal of Propulsion and Power, 1993,

9(4): 499-514.

[60] Bogdanoff D W. Advanced injection and mixing techniques for scramjet combustors[J]. Journal of Propulsion and Power, 1994, 10(2): 183-190.

[61] Bushnell D M. Hypervelocity scramjet mixing enhancement[J]. Journal of Propulsion and Power, 1995, 11(5): 1088-1090.

[62] Ton, V. T., Karagozian, A. R., Marble, F. E., Osher, S. J., & Engquist, B. E. Numerical simulations of high-speed chemically reacting flow[J]. Theoretical and Computational Fluid Dynamics, 1994, 6(2-3): 161-179.

[63] Lee S H, Jeung I S, Yoon Y. Computational investigation of shock-enhanced mixing and combustion[J]. AIAA journal, 1997, 35(12): 1813-1820.

[64] Cecere, D., Ingenito, A., Giacomazzi, E., Romagnosi, L., & Bruno, C. Hydrogen/air supersonic combustion for future hypersonic vehicles[J]. International Journal of Hydrogen Energy, 2011, 36(18): 11969-11984.